Analysis of translating mitoribosome reveals functional characteristics of protein synthesis in mitochondria of fungi

Yuzuru Itoh[1,2†], Andreas Naschberger[1†], Narges Mortezaei[1†], Johannes Herrmann[3] and Alexey Amunts[1,2*]

[1]Science for Life Laboratory, Department of Biochemistry and Biophysics, Stockholm University, 17165 Solna, Sweden

[2]Department of Medical Biochemistry and Biophysics, Karolinska Institutet, 17165 Solna, Sweden

[3]Cell Biology, University of Kaiserslautern, Erwin-Schrödinger-Straße 13, 67663 Kaiserslautern, Germany

† These authors contributed equally to this work.

* email: amunts@scilifelab.se

Abstract

Mitoribosomes have been specialized for protein synthesis in mitochondria. While it is established that mitoribosomes differ between species, a reference model from the Fungi kingdom is missing, and the structural basis for the mitoribosomal function is not understood. We report models of the translating fungal mitoribosome with mRNA, tRNA and nascent polypeptide, as well as an assembly intermediate, determined from cryo-EM maps at overall resolution of 2.98-3.09 Å. Most of the rRNA expansion segments were modeled, and five additional associated proteins were identified. Collectively, the expanded rRNA and mitochondria-specific protein elements coordinate binding of nicotinamide adenine dinucleotide (NAD) in the central protuberance of the large subunit and the ATPase inhibitory factor 1 (IF_1) in the small subunit. The models of the active fungal mitoribosome explain how mRNA binds through a dedicated protein platform on the small subunit, tRNA translocated with the help of newly identified protein mL108, bridging it with L1 stalk on the large subunit, and nascent polypeptide paths through the exit tunnel involving a series of conformational rearrangements. Finally, an assembly intermediate is found and modeled with the maturation factor Atp25, providing insight into the biogenesis of the mitoribosomal large subunit and translation regulation.

Proteins synthesis in mitochondria supports bioenergetics of eukaryotic cells and executed by dedicated mitoribosomes. Cryo-EM has been instrumental in revealing the first structural snapshots of mitoribosomes. While for mammals the obtained models from human embryonic kidney cells[1,2] are in agreement with those from porcine and bovine tissues[3,4], the structure of the mitoribosome from the yeast *Saccharomyces cerevisiae* displayed considerable specializations[5,6]. Particularly, it proposed a distinct composition and putative deviations in the functionally defining features of translation, including an expanded mRNA channel exit and rerouted polypeptide exit channel.

Although the cryo-EM data is informative, the deviations of the mitoribosome from a single-celled *S. cerevisiae* that lacks complex I cannot be considered as a prototypic example, but more likely species-specific. In addition, the available models are incomplete due to the limited resolution. Functionally, since the models were derived from dormant mitoribosomes, without tRNA bound to mRNA and nascent polypeptide, the mechanism of action and roles of specific proteins could not be understood. Therefore, in the absence of high-resolution structural information of translating mitoribosome, key questions regarding mitochondrial translation remain open. To provide a representative reference for studying protein synthesis in the mitochondria of fungi, and to reveal how the mitoribosome functions in coordination with its translation partners, we determined structures of the translating mitoribosome from the representative fungal model organism *Neurospora crassa.*

N. crassa has been recognized as the organism used for answering a variety of fundamental biological questions, including in the field of mitochondrial translation. This includes early characterization of the physicochemical properties of the mitoribosomes and the base composition of its rRNA[7], the finding that mitoribosomal intactness requires a relatively high magnesium concentration[8], studies showing radioactive amino acid incorporation into mitoribosome[9], the finding that Oxa1 facilitates integration of mitochondrially encoded proteins into the inner membrane[10], and the first evolutionary analysis of the mitoribosome[11]. Following these considerations, to provide a reference for the process of protein synthesis in mitochondria, we set to investigate the translation apparatus from the model organism filamentous fungus *N. crassa.*

Structure determination

In order to characterize a representative functional mitoribosome, the *N. crassa* mycelia of the strain K5-15-23-1 overexpressing the protein Oxa1[10] were grown aerobically, and translation was stalled using chloramphenicol prior to harvesting. The mycelia were dried, lysed with mortar and pestle, and the mitoribosomes were purified as described previously[12], and subjected to cryo-EM analysis. The cryo-EM consensus map was obtained from 131,806 particles at overall resolution of 2.86 Å (Supplementary Fig. 1).

The 3D classification resulted in two reconstructions of the mitoribosome corresponding to the ratcheted and non-ratcheted states (Supplementary Fig. 1). After subtracting the mitoribosome signals outside the tRNA binding sites, followed by focus 3D classifications, we obtained three

distinct classes of mitoribosome with a tRNA occupying P-site (P/P), E-site (E/E), and in the hybrid P/E state, at the overall resolutions of 3.05, 3.09, and 2.98 Å, respectively (Supplementary Fig. 1). In the P/P and P/E tRNA states, we detected and modeled co-purified native mitochondrial mRNA, and the density corresponding to the nascent polypeptide was identified.

To further improve the local resolution, focused masked refinements were performed using the masks for the large subunit (mtLSU) core, central protuberance (CP), L1 stalk, uL10m region, the small subunit (mtSSU) head, body and tail (Supplementary Fig. 2-4). Consequently, the resolution was improved to ~2.50-3.40 Å throughout most of the regions. The quality of the maps allowed building the most complete available model, including identification of five proteins previously missed: uL1m, uL10m, uL11m, mL53 and mL54; two newly identified mitoribosomal proteins: mL108 and the ATP synthase inhibitory factor 1 (IF_1); and 60 proteins with higher completeness, as well as the rRNAs (Fig. 1a, Supplementary Figs 6-8).

In addition, we noted that mitoribosomes from actively growing *N. crassa* mycelia contain a pool of free mtLSU (Supplementary Fig. 5), which resembles the profile of assembly intermediate reported from the mitochondria of human embryonic kidney cells[13]. Unlike the mtLSU in the intact mitoribosome, this population missing the density for bL9m, but has an extra factor Atp25 bound to uL14m, and a poor density at the interface consistent with unfolded mt-rRNA. The quality of the structural data allowed analyzing the differences with the mature mtLSU, and propose a putative regulatory mechanism.

Overall structure and new features

The fungal mitoribosome consists of 78 different proteins, 23S and 16S rRNAs (Fig. 1, Supplementary Figs 6-8, Supplementary Tables 1 and 2). The proteins mS42 and IF_1 are found in two copies as homodimers. 48 bacterial orthologs are extended, and 30 proteins are mitochondria specific . For the rRNA, we modeled 16 expansion segments (ES), 15 of which are in the mtLSU (Supplementary Figs. 6-8), and several other rRNA regions have been reduced. The deletion in the mtDNA genome are not correlated with a specific functional feature or attributed to selective loss/gain of activity, but rather reflect a general reductive phase in the mitochondrial genome[11]. For the native mitochondrial tRNAs (P/P, P/E, E/E states) and mRNA, we modeled nucleotide sequences that fit the corresponding densities the best, because those densities represent a mixture of different tRNAs and mRNAs in mitochondria.

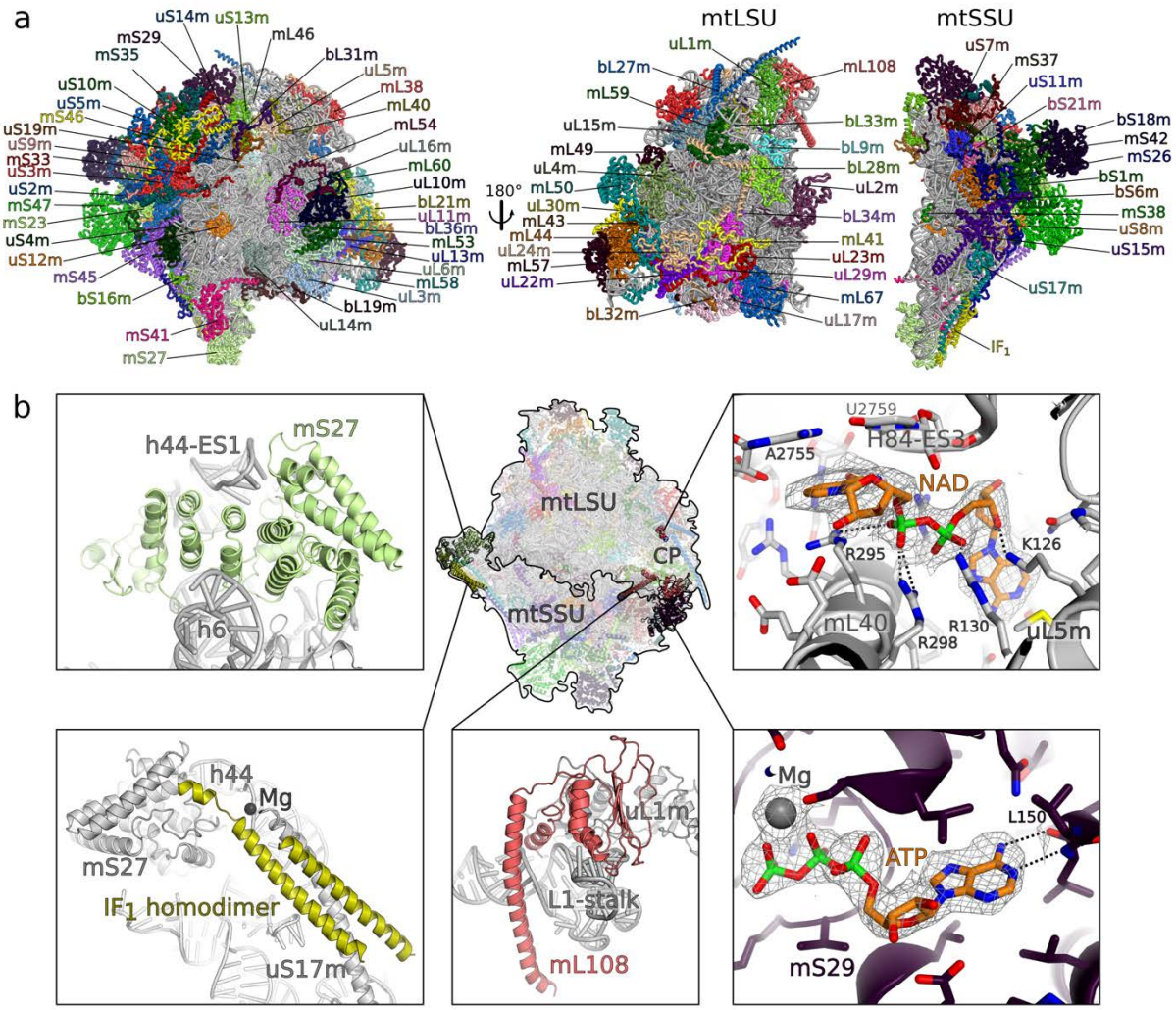

Figure 1: Structure of the fungal mitoribosome and new features. a, Overall structure of the complete mitoribosome and its subunits with indicated mitoribosomal proteins. **b, Top left:** Remodeled and reannotated mS27 interacts with h44-ES1.**Bottom left:** Newly identified mitoribosomal component IF_1 homodimer bound to h44-ES1 and uS17m extension**;Top right** NAD binding pocket in the CP formed by uL5m, mL40, and H84-ES3.**Bottom center:** Newly identified mitoribosomal component mL108 is located in the L1 stalk**;Bottom right:** Nucleotide binding pocket of mS29 bound with chemically favorable ATP shown with its density.

Some of the improvements in the model due to the high-resolution map are exemplified in Figure 1. Protein mS27, which was previously partially built as poly-Ala, has been identified directly from the density as helical repeat protein consistently with mammalian counterparts. We named it accordingly mS27 (previously mS44) (Fig. 1b, Supplementary Fig. 9 and Supplementary Table 2). Another example is the protein mS29 that was reported as a GTPase involved in apoptosis, and mutations in the P-loop motif of the nucleotide binding pocket were suggested to impair this function[14]. In the nucleotide pocket of mS29, which was previously modeled with guanosine diphosphate (GDP), we can see at the local resolution of 2.77 Å that the density for N2 purine ring atom is missing, and the correct assignment for the nucleotide is adenosine triphosphate

(ATP) (Fig. 1b). This is further supported by the better resolved chemical environment formed by Leu150 of mS29, which would be incompatible with guanine since the O6 carbonyl of guanine imparts repulsive interaction with the backbone carbonyl of Leu150 (acceptor with acceptor), and the NH1 group of guanine forms a second repulsive interaction with the backbone NH group of Leu150 (donor with donor). Placing an ATP instead of GDP leads to favorable interactions. Therefore, the structure shows no evidence of mS29 being a GTPase in fungi.

In the CP, we found NAD in the binding pocket formed by mL40, uL5m, and rRNA H84-ES3 (Fig. 1b). Positively charged residues of mL40 and uL5m interact with the negatively charged NAD phosphates. The pyridine ring of the nicotinamide is held in place by π-stacking on the base pair of A2755 and U2759. Arg295 of mL40 forms π-stacking at the other side of the NAD pyridine. Therefore, NAD bridges the mitoribosomal proteins and the mt-rRNA at the core of CP. This implies regulatory function in the assembly of the mtLSU based on the local NAD level.

The natural inhibitor of the mitochondrial ATP synthase IF_1 is bound to the mtSSU tail as a homodimer, which is its active state (Fig. 1b). IF_1 inhibits the ATP synthase activity by inserting its N-terminal part into the catalytically active F_1 domain, thereby blocking its rotational movement and subsequently its hydrolase and synthase activities[15]. The mtSSU-bound IF_1 was identified directly from the density, due to the characteristic coiled-coil homodimerization of the C-terminal helix and side-chain fitting. It binds to the h44 rRNA, mS27, and the C-terminal extension of uS17m that forms a helical bundle with the coiled-coil (Fig. 1b). A metal ion Mg^{2+} bridges a backbone phosphate of h44 with uS17m and IF_1. The topology of IF_1 is such that N- and C-termini of each monomer point in the opposite direction: one towards the mtSSU body, and the other towards the solvent. The latter appears to have a similar conformation to the canonical binding on the ATP synthase. Since h44 is expanded and coordinated by uS17m extension, it suggests that IF_1 has been acquired through the mechanism of 'structural patching' to stabilize the rapidly evolving growth[16]. Functionally, IF_1 may link the biogenesis of mitoribosome to the ATP synthesis assembly and inhibition.

Mechanism of mRNA binding involving a dedicated protein platform

Focused classifications on the tRNA binding sites yielded structures of three distinct classes with bound tRNA in P/P, P/E, E/E (Supplementary Fig. 1). The quality of the density allowed us to generate structural models of the translating mitoribosomal complexes with P/P and P/E tRNAs. The presence of tRNAs correlates with additional density lining the mRNA channel path, where well resolved map allowed modeling 10 nucleotides of the native mRNA. The codon-anticodon base pairings are observed in the density of the P/P and P/E states (Fig. 2b). The decoding center is conserved, including the position of the flipped-out bases A1803 (A1492 in *E. coli*), A1804 (A1493) and G756 (G530), as well as the curvature in mRNA around h28. In addition to the modeled mRNA nucleotides in the channel, bulky density extends upstream to the channel entry and downstream to its exit. Therefore, the map allows us to determine how mRNA binds to the mitoribosome and to trace its complete path.

162 The reference point to the channel entry is the universal site formed by uS3m, uS4m and uS5m.
163 Compared to the previously determined structures of bacterial complex, mRNA contacts
164 mitochondria-specific mS35 as well. However, the density for the mRNA chain starts prior the
165 conventional entry. Particularly, following the density, we observe extended structure involving
166 mitochondria-specific extensions of uS3m and uS5m that are held together at the mtSSU head by
167 mS35 and mS46 (Fig. 2a). This architecture is coupled to the mRNA terminus, thereby
168 suggesting a potential platform for its loading on to the mitoribosome. The formed loading
169 platform narrows the entry site considerably, ensuring that the mRNA entering the channel is
170 unpaired. Interestingly, two mitochondria specific proteins mS26 and mS35 extend along the
171 mRNA channel from its entry region to the opposite mtSSU pole, where the exit site is, providing
172 a structural continuum (Fig. 2b).

173 The channel exit site typically resides at the 3′ end of the rRNA. In the fungal mitoribosome, it
174 has not been significantly altered. The remodeling reported in *S. cerevisiae* does not occur, and
175 therefore represents either a dormant state or species-specific feature. In addition to the conserved
176 proteins, mitochondria-specific mS23, mS26 and mS37 shape the path for mRNA movement
177 (Fig. 2c). The C-terminal extension of uS7m narrows the channel, and protein bS18m, mS23,
178 mS26 and mS37 interact with the mRNA density directly. The path toward the exit appears to
179 divaricate, and each subway could in principle accommodate a single stranded mRNA. However,
180 the density for the 5′ mRNA clearly follows only the path lateral to mS26 that is also surrounded
181 by a positively charged chemical environment . Protein bS1m, which is considered to have one of
182 the most conserved and ancient protein domains with functional importance of unfolding mRNAs
183 for active translation[17], is permanently bound to the channel exit (Fig. 2c).

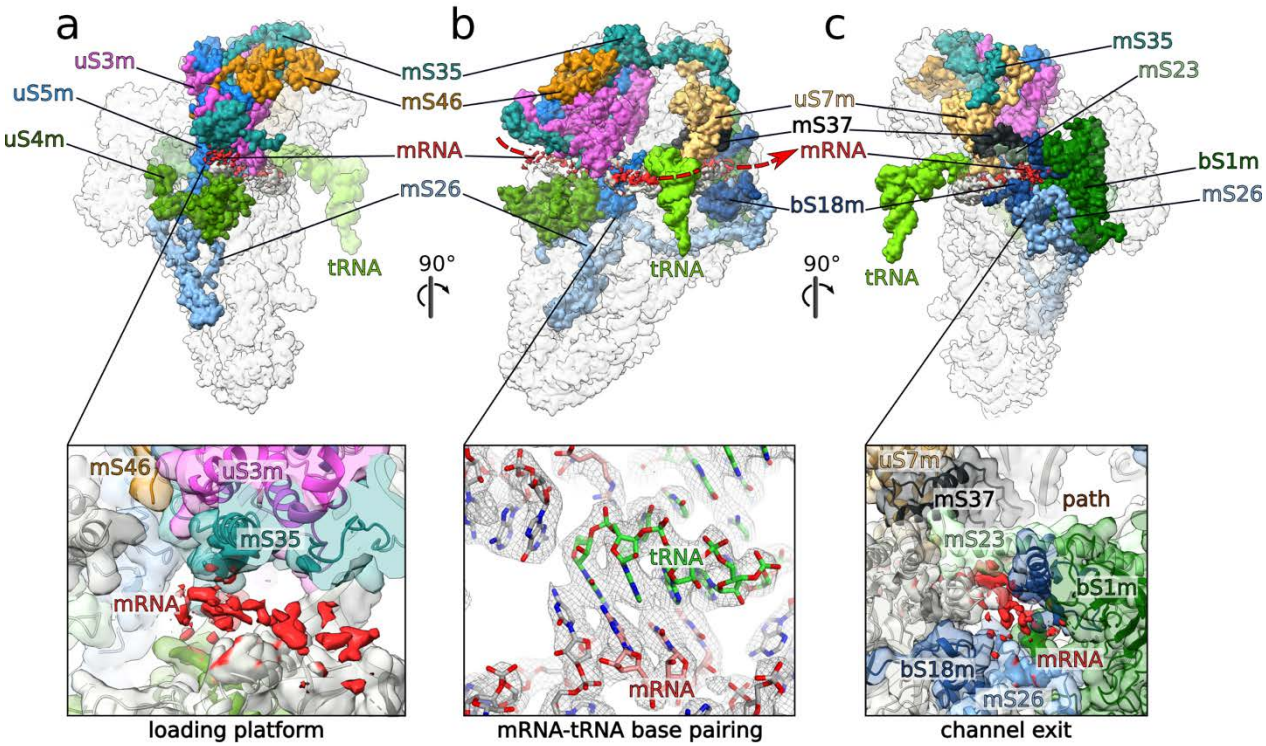

Figure 2: The mRNA channel traced with the density. a, The density for mRNA (red) reveals a protein platform formed by mS35, mS46 and extensions of uS3m and uS5m. **b,** The overall path taken by mRNA is indicated based on the additional density associated with the mtSSU, and codon-anticodon base pairings at the decoding center shown with density. **c,** At the exit site, proteins uS7m, bS18m, mS23, mS26 and mS37 are in contact with mRNA, and bS1m is permanently bound. A putative alternative path is indicated.

Mechanism of tRNA translocation involving a new protein in L1 stalk

During translation, tRNAs are translocated between the three sites. Upon peptide-bond formation, the ribosomal subunits rotate with respect to each other, and the tRNA moves to the intermediate hybrid state. The structure comparison between the complexes with P/P and P/E tRNAs reveals sequential rearrangements in the network of mitoribosome-tRNA interactions and allows us to determine how tRNA is translocated.

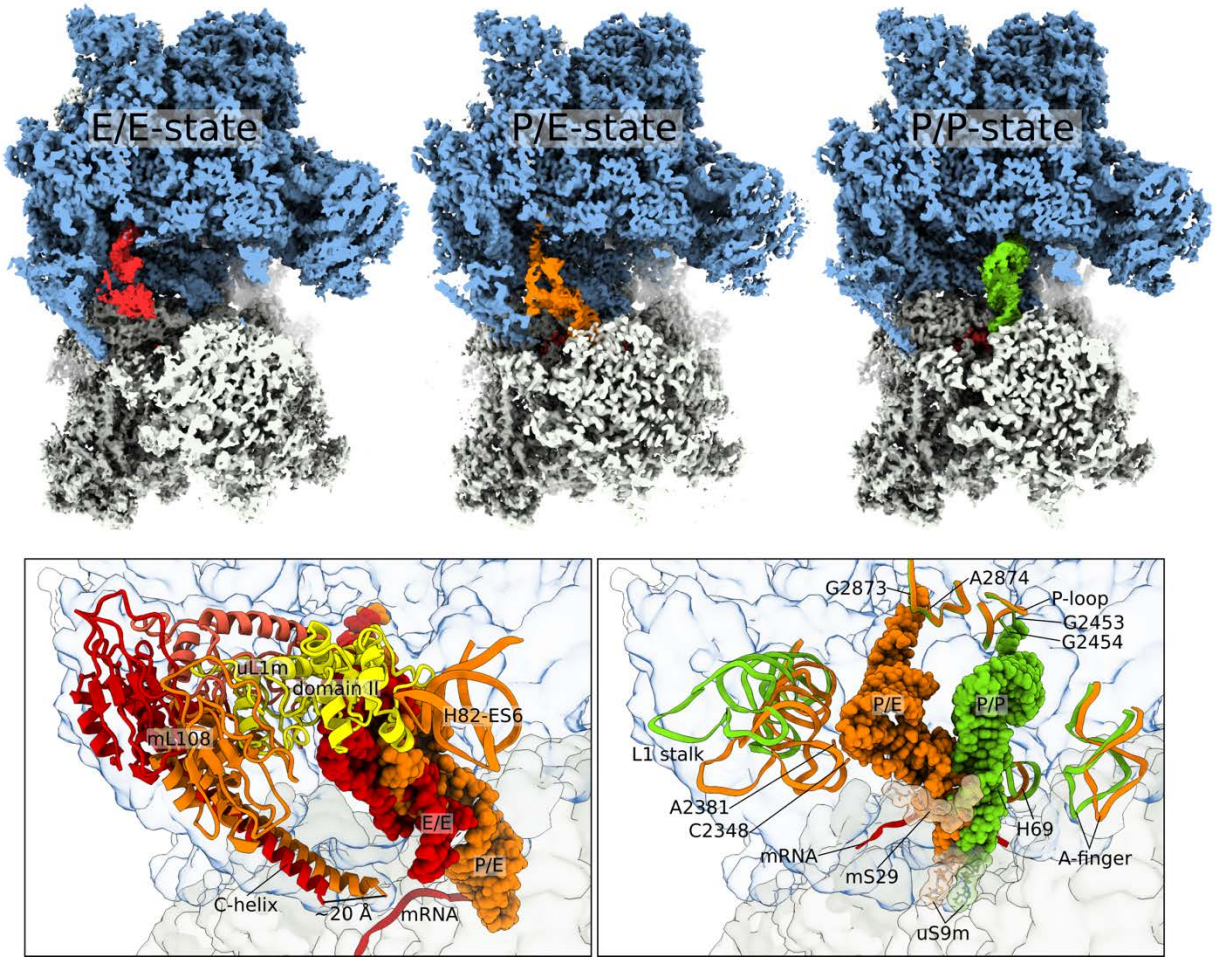

Figure 3: Translocation of tRNA and the L1 stalk. 3D reconstructions of the different states are shown in the top panel (mtLSU blue; mtSSU gray). Structural rearrangements upon transition between the three states are shown in the bottom panels (right: P/P to P/E; left: P/E to E/E). Each two states have been superimposed, and the affected structural elements are shown according to the text.

In the P/P state the anticodon of the tRNA forms base pairing with the mRNA in the conserved P-site of the mtSSU (Fig. 3 and Supplementary Fig. 10). Further stabilization is provided by the conserved C-terminal Arg315 of uS9m, which forms salt bridges with the backbone phosphates in the anticodon loop of the tRNA. The conserved H69 of mtLSU interacts with the D-arm of the tRNA. The conformation of P/P tRNA is overall similar to bacteria. The A-site finger, known as a functional attenuator and important for keeping the correct reading frame[18], takes in a straight conformation forming the inter-subunit bridge B1a. The conserved G2453 (G2251) and G2454 (G2252) of the P-loop form base pairs with the CCA terminus of the tRNA and the emerging peptide is bound to the terminal A76, waiting for peptidyl transfer to the next incoming aminoacyl-tRNA at the A-site. Thus, the arrangement of structural elements and tRNA in mitochondria of fungi shows a conserved P-site.

After peptide transfer occurs, the ribosomal subunits move relative to each other forming ratcheted conformation coupled with tRNA translocation, which is represented by our P/E hybrid structure. In the ratcheted conformation, the L1 stalk moves to a closed conformation toward the deacylated tRNA in the P/E hybrid state (Fig. 3). By masked refinement on L1 stalk, we improved the density that allowed building its complete model for the first time in any mitoribosome. We identified additional protein component, namely mL108 (Fig. 1b and Supplementary Fig. 11), which is unprecedented occurrence in cytoplasmic counterparts. The core of the protein shows a thioredoxin-like fold, which belongs to a small folding family including mS25, mL43, and the complex I subunit NDUFA2/B8. All these proteins are specific to mitochondria, bearing the possibility of a shared evolutional origin. The protein mL108 interacts with both the L1-stalk rRNA and the protein uL1m (Fig. 3). Furthermore, it forms a new inter-subunit bridge with a long C-terminal helix (Fig. 3).

The bases A2381 (G2168) and C2348 (G2112) of the stalk rRNA stack on the elbow of the P/E tRNA (Fig. 3). Unlike in bacteria, uL1m does not interact with the P/E tRNA, instead the domain II of uL1m changes its conformation to form a mitoribsome specific interaction with H82-ES1 in the CP in the ratcheted state (Fig. 3). Therefore, the subunit rotation is synchronized with the L1 stalk movement during tRNA translocation. The terminal adenosine of the P/E tRNA inserts between the conserved G2873 (G2421) and A2874 (C2422) at the E site (Fig. 3). The anticodon arm of the tRNA remains located in the P site forming the codon-anticodon base pairing with the mRNA, resulting in distorted conformation, to swing the acceptor arm into the E-site. The disordered N-terminal extension of mS29 gets structured in the ratcheted state and interacts to the minor groove of the anticodon stem of the P/E tRNA (Supplementary Fig. 10), suggesting mitochondria-specific regulation of the translation mechanism. The long C-terminal helix of mL108 reaches down to the mtSSU, applying an additional stabilization of the L1 stalk.

Upon back rotation of the mtSSU into the non-ratcheted E/E state, the L1 stalk moves outwards assisting to pull the P/E tRNA into the E/E state, allowing dissociation into the solvent to complete the translocation cycle (Fig. 3 and Supplementary Fig. 10). The protein uL1m thereby detaches from the CP, releasing the domain II of uL1m. The tip of the C-terminal helix of mL108 translates ~20 Å forming a new bridge with mtSSU by slightly changing its curvature. This structural rearrangement during mtSSU rotation suggests for a mitochondria-specific ratchet sensing mechanism that coordinates the movement of the mtSSU rotation via mL108 to the L1 stalk.

Taken together, the data enables to derive a mechanism for the tRNA translocation describing a series of key conformational changes of the mitoribosomes and its ligands. First, the L1 stalk interacts with mtSSU through mL108 thereby sensing the rotation state. This leads to the inward moving of the rRNA part of the L1 stalk to interact with the tRNA. The domain II of uL1m stabilizes the conformation through the mitochondria-specific interactions with the CP, and mS29 N-terminal loop becoming ordered and stabilizes the tRNA in the P/E state, which is disrupted in the following E/E state.

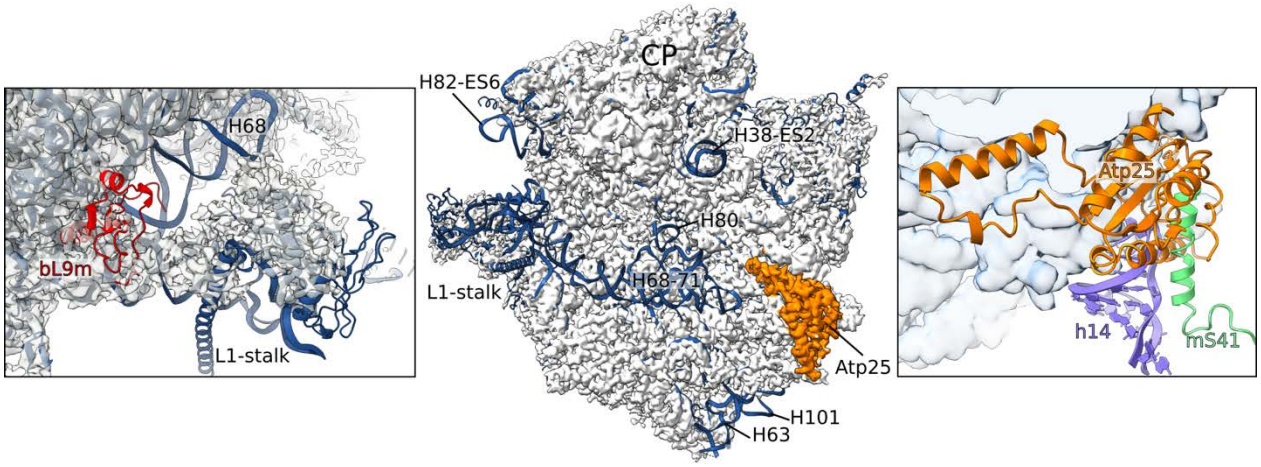

Figure 4: Structure and function of the mtLSU-Atp25 assembly complex. Superposition of the assembly intermediate cryo-EM map (gray) with the mature mtLSU model (blue) reveals unfolded interfacial rRNA, conformational change of the L1 stalk (left panel), missing bL9m (red), presence of Atp25 (orange) that would clash with the mt SSU h14 and mS41, preventing subunit association.

Visualization of mtLSU-Atp25 assembly intermediate suggests regulatory mechanism

During 3D classification, we recognized a minor population of the particles corresponding to the isolated mtLSU, and subsequent processing resulted in 3.03 Å resolution reconstruction from 24,142 particles (Supplementary Fig. 5). Fitting the mtLSU model revealed an extra density that appears as a protein element forming a heterodimer with uL14m. In addition, rRNA at the interface (38-ES2, H63, H67-71, H80, 82-ES6, H101, PTC) appears as unfolded (Fig. 4). Further, the L1 stalk changes to conformation that is more flexible and the density for bL9m next to L1 stalk is absent, whereas all the other mtLSU proteins are present (Fig. 4).

We identified the extra density as Atp25, an ortholog of the bacterial ribosome silencing factor (Rsf), for which there is no high-resolution structural information in complex with a ribosome[19,20]. Its human mitochondrial counterpart MALSU1 has been shown to involve late assembly stages[13,21]. The gene *Atp25* codes for 699 amino acids, including the targeting sequence, N-terminal part related to Rsf/MALSU1, and C-terminal part called the M-domain. In *S. cerevisiae*, ATP25 is cleaved between the N- and C-terminal parts during mitochondrial import [22], and the M-domain forms a separate functional protein that stabilizes the mRNA of the ATP synthase subunit Atp9p[23]. The gene fusion is suggested to have evolved in order to prevent off target effects of Atp25 on the cytosolic ribosomes prior entry to mitochondria[22]. We observe only the Rsf/MALSU1-related part of Atp25 on the mitoribosome, confirming the function in the assembly of the mtLSU.

Visualization of the mtLSU-Atp25 complex provides structural basis for the assembly pathway and insight into possible regulation of translation in mitochondria. Atp25 presents only in the class with the missing bL9m and unfolded interfacial rRNA that affects the L1 stalk. In the

mature mitoribosome, bL9m is anchored at the base of the L1 stalk near the E-site, which is stabilized through tertiary interactions with the rRNA. Therefore, the recruitment of bL9m requires specific L1 stalk conformation that is interdependent with rRNA folding, including the PTC. Indeed, ribosomes purified from bL9-deficient strain of *E. coli* show increased susceptibility to aminoglycosides[24], and the folding of the PTC is among the last maturation events[25,26]. Furthermore, bacterial ribosomes lacking bL9 exhibit increased frameshifting[27-29], for which the molecular mechanism has been proposed recently through transiently stalled compacted ribosomes[30].

Atp25 bound to uL14m sterically obstruct the binding of the mtSSU by preventing the formation of bridge B8 with its globular domain (Fig. 4). The steric block spans ~25 Å, would clash with h14 of rRNA and the N terminus of mS26 of the mtSSU. Therefore, the eviction of Atp25 must take place during the final stages of maturation to alleviate the steric hindrance on subunit joining. A similar mechanism was proposed for eIF6 in the cytoplasmic translation apparatus, where protein factor SBDS senses the structural integrity of the functional sites before the displacement[31]. Our data imply that since this is a prerequisite step for the folding of interfacial mt-rRNA into a native-like conformation, it is also a requirement for the binding of bL9m. This shows that bL9m attachment is mechanistically regulated during the assembly of the mitoribosome. Since bL9 suppresses frameshifting in bacteria, the structure of the mtLSU-Atp25 lacking bL9m suggests regulation of frameshifting in mitochondrial translation, which might be important for fidelity and reflects an adaptation to the mitochondrial mRNAs.

References

1 Brown, A. *et al.* Structure of the large ribosomal subunit from human mitochondria. *Science* **346**, 718-722, doi:10.1126/science.1258026 (2014).

2 Amunts, A., Brown, A., Toots, J., Scheres, S. H. W. & Ramakrishnan, V. Ribosome. The structure of the human mitochondrial ribosome. *Science* **348**, 95-98, doi:10.1126/science.aaa1193 (2015).

3 Greber, B. J. *et al.* Architecture of the large subunit of the mammalian mitochondrial ribosome. *Nature* **505**, 515-519, doi:10.1038/nature12890 (2014).

4 Greber, B. J. *et al.* Ribosome. The complete structure of the 55S mammalian mitochondrial ribosome. *Science* **348**, 303-308, doi:10.1126/science.aaa3872 (2015).

5 Amunts, A. *et al.* Structure of the yeast mitochondrial large ribosomal subunit. *Science* **343**, 1485-1489, doi:10.1126/science.1249410 (2014).

6 Desai, N., Brown, A., Amunts, A. & Ramakrishnan, V. The structure of the yeast mitochondrial ribosome. *Science* **355**, 528-531, doi:10.1126/science.aal2415 (2017).

7 Kuntzel, H. & Noll, H. Mitochondrial and cytoplasmic polysomes from Neurospora crassa. *Nature* **215**, 1340-1345, doi:10.1038/2151340a0 (1967).

8 Kuntzel, H. Mitochondrial and cytoplasmic ribosomes from Neurospora crassa: characterization of their subunits. *J Mol Biol* **40**, 315-320, doi:10.1016/0022-2836(69)90481-1 (1969).

9 Neupert, W., Sebald, W., Schwab, A. J., Massinger, P. & Bucher, T. Incorporation in vivo of 14C-labelled amino acids into the proteins of mitochondrial ribosomes from

Neurospora crassa sensitive to cycloheximide and insensitive to Chloramphenicol. *Eur J Biochem* **10**, 589-591, doi:10.1111/j.1432-1033.1969.tb00730.x (1969).

10 Nargang, F. E., Preuss, M., Neupert, W. & Herrmann, J. M. The Oxa1 protein forms a homooligomeric complex and is an essential part of the mitochondrial export translocase in Neurospora crassa. *J Biol Chem* **277**, 12846-12853, doi:10.1074/jbc.M112099200 (2002).

11 van der Sluis, E. O. *et al.* Parallel Structural Evolution of Mitochondrial Ribosomes and OXPHOS Complexes. *Genome Biol Evol* **7**, 1235-1251, doi:10.1093/gbe/evv061 (2015).

12 Aibara, S., Andrell, J., Singh, V. & Amunts, A. Rapid Isolation of the Mitoribosome from HEK Cells. *J Vis Exp*, doi:10.3791/57877 (2018).

13 Brown, A. *et al.* Structures of the human mitochondrial ribosome in native states of assembly. *Nat Struct Mol Biol* **24**, 866-869, doi:10.1038/nsmb.3464 (2017).

14 Kim, H. J., Maiti, P. & Barrientos, A. Mitochondrial ribosomes in cancer. *Semin Cancer Biol* **47**, 67-81, doi:10.1016/j.semcancer.2017.04.004 (2017).

15 Esparza-Molto, P. B., Nuevo-Tapioles, C. & Cuezva, J. M. Regulation of the H(+)-ATP synthase by IF1: a role in mitohormesis. *Cell Mol Life Sci* **74**, 2151-2166, doi:10.1007/s00018-017-2462-8 (2017).

16 Petrov, A. S. *et al.* Structural Patching Fosters Divergence of Mitochondrial Ribosomes. *Mol Biol Evol* **36**, 207-219, doi:10.1093/molbev/msy221 (2019).

17 Qu, X., Lancaster, L., Noller, H. F., Bustamante, C. & Tinoco, I., Jr. Ribosomal protein S1 unwinds double-stranded RNA in multiple steps. *Proc Natl Acad Sci U S A* **109**, 14458-14463, doi:10.1073/pnas.1208950109 (2012).

18 Komoda, T. *et al.* The A-site finger in 23 S rRNA acts as a functional attenuator for translocation. *J Biol Chem* **281**, 32303-32309, doi:10.1074/jbc.M607058200 (2006).

19 Hauser, R. *et al.* RsfA (YbeB) proteins are conserved ribosomal silencing factors. *PLoS Genet* **8**, e1002815, doi:10.1371/journal.pgen.1002815 (2012).

20 Li, X. *et al.* Structure of Ribosomal Silencing Factor Bound to Mycobacterium tuberculosis Ribosome. *Structure* **23**, 2387, doi:10.1016/j.str.2015.11.002 (2015).

21 Rorbach, J., Gammage, P. A. & Minczuk, M. C7orf30 is necessary for biogenesis of the large subunit of the mitochondrial ribosome. *Nucleic Acids Res* **40**, 4097-4109, doi:10.1093/nar/gkr1282 (2012).

22 Woellhaf, M. W., Sommer, F., Schroda, M. & Herrmann, J. M. Proteomic profiling of the mitochondrial ribosome identifies Atp25 as a composite mitochondrial precursor protein. *Mol Biol Cell* **27**, 3031-3039, doi:10.1091/mbc.E16-07-0513 (2016).

23 Zeng, X., Barros, M. H., Shulman, T. & Tzagoloff, A. ATP25, a new nuclear gene of Saccharomyces cerevisiae required for expression and assembly of the Atp9p subunit of mitochondrial ATPase. *Mol Biol Cell* **19**, 1366-1377, doi:10.1091/mbc.E07-08-0746 (2008).

24 Naganathan, A., Wood, M. P. & Moore, S. D. The large ribosomal subunit protein L9 enables the growth of EF-P deficient cells and enhances small subunit maturation. *PLoS One* **10**, e0120060, doi:10.1371/journal.pone.0120060 (2015).

25 Li, N. *et al.* Cryo-EM structures of the late-stage assembly intermediates of the bacterial 50S ribosomal subunit. *Nucleic Acids Res* **41**, 7073-7083, doi:10.1093/nar/gkt423 (2013).

26 Jomaa, A. *et al.* Functional domains of the 50S subunit mature late in the assembly process. *Nucleic Acids Res* **42**, 3419-3435, doi:10.1093/nar/gkt1295 (2014).

27 Atkins, J. F., Loughran, G., Bhatt, P. R., Firth, A. E. & Baranov, P. V. Ribosomal frameshifting and transcriptional slippage: From genetic steganography and cryptography to adventitious use. *Nucleic Acids Res* **44**, 7007-7078, doi:10.1093/nar/gkw530 (2016).

28 Herr, A. J., Nelson, C. C., Wills, N. M., Gesteland, R. F. & Atkins, J. F. Analysis of the roles of tRNA structure, ribosomal protein L9, and the bacteriophage T4 gene 60 bypassing signals during ribosome slippage on mRNA. *J Mol Biol* **309**, 1029-1048, doi:10.1006/jmbi.2001.4717 (2001).

29 Seidman, J. S., Janssen, B. D. & Hayes, C. S. Alternative fates of paused ribosomes during translation termination. *J Biol Chem* **286**, 31105-31112, doi:10.1074/jbc.M111.268201 (2011).

30 Smith, A. M., Costello, M. S., Kettring, A. H., Wingo, R. J. & Moore, S. D. Ribosome collisions alter frameshifting at translational reprogramming motifs in bacterial mRNAs. *Proc Natl Acad Sci U S A* **116**, 21769-21779, doi:10.1073/pnas.1910613116 (2019).

31 Weis, F. *et al.* Mechanism of eIF6 release from the nascent 60S ribosomal subunit. *Nat Struct Mol Biol* **22**, 914-919, doi:10.1038/nsmb.3112 (2015).

32 Funes, S., Nargang, F. E., Neupert, W. & Herrmann, J. M. The Oxa2 protein of Neurospora crassa plays a critical role in the biogenesis of cytochrome oxidase and defines a ubiquitous subbranch of the Oxa1/YidC/Alb3 protein family. *Mol Biol Cell* **15**, 1853-1861, doi:10.1091/mbc.e03-11-0789 (2004).

33 Vogel, H. J. A Convenient Growth Medium for Neurospora crassa. *Microbial Genet. Bull.* **13**, 42-43 (1956).

34 Li, X. *et al.* Electron counting and beam-induced motion correction enable near-atomic-resolution single-particle cryo-EM. *Nat Methods* **10**, 584-590, doi:10.1038/nmeth.2472 (2013).

35 Zhang, K. Gctf: Real-time CTF determination and correction. *J Struct Biol* **193**, 1-12, doi:10.1016/j.jsb.2015.11.003 (2016).

36 Kimanius, D., Forsberg, B. O., Scheres, S. H. & Lindahl, E. Accelerated cryo-EM structure determination with parallelisation using GPUs in RELION-2. *Elife* **5**, doi:10.7554/eLife.18722 (2016).

37 Zivanov, J. *et al.* New tools for automated high-resolution cryo-EM structure determination in RELION-3. *Elife* **7**, doi:10.7554/eLife.42166 (2018).

38 Zivanov, J., Nakane, T. & Scheres, S. H. W. A Bayesian approach to beam-induced motion correction in cryo-EM single-particle analysis. *IUCrJ* **6**, 5-17, doi:10.1107/S205225251801463X (2019).

39 Emsley, P. & Cowtan, K. Coot: model-building tools for molecular graphics. *Acta Crystallogr D Biol Crystallogr* **60**, 2126-2132, doi:10.1107/S0907444904019158 (2004).

40 Pettersen, E. F. *et al.* UCSF Chimera--a visualization system for exploratory research and analysis. *J Comput Chem* **25**, 1605-1612, doi:10.1002/jcc.20084 (2004).

41 Waterhouse, A. *et al.* SWISS-MODEL: homology modelling of protein structures and complexes. *Nucleic Acids Res* **46**, W296-W303, doi:10.1093/nar/gky427 (2018).

42 Altschul, S. F., Gish, W., Miller, W., Myers, E. W. & Lipman, D. J. Basic local alignment search tool. *J Mol Biol* **215**, 403-410, doi:10.1016/S0022-2836(05)80360-2 (1990).

43 Ban, N. *et al.* A new system for naming ribosomal proteins. *Curr Opin Struct Biol* **24**, 165-169, doi:10.1016/j.sbi.2014.01.002 (2014).

44 Liebschner, D. *et al.* Macromolecular structure determination using X-rays, neutrons and electrons: recent developments in Phenix. *Acta Crystallogr D Struct Biol* **75**, 861-877, doi:10.1107/S2059798319011471 (2019).

45 Afonine, P. V. *et al.* Real-space refinement in PHENIX for cryo-EM and crystallography. *Acta Crystallogr D Struct Biol* **74**, 531-544, doi:10.1107/S2059798318006551 (2018).
46 Williams, C. J. *et al.* MolProbity: More and better reference data for improved all-atom structure validation. *Protein Sci* **27**, 293-315, doi:10.1002/pro.3330 (2018).
47 DeLano, W. L. Pymol: An open-source molecular graphics tool. . *CCP4 Newsletter On Protein Crystallography* **40**, 82-92 (2002).
48 Goddard, T. D. *et al.* UCSF ChimeraX: Meeting modern challenges in visualization and analysis. *Protein Sci* **27**, 14-25, doi:10.1002/pro.3235 (2018).

427

428 # Methods

429 **Purification of mitoribosomes**

430 Mitochondria were isolated from *Neurospora crassa* strain K5-15-23-1[32] which contains a His-
431 tagged version of Oxa1. The *N. crassa* mycelia were grown in aerobic conditions using 10 L of
432 the Vogel's growth medium[33], supplemented with L-lysine and L-leucine at 25°C for 16 h. Each
433 growth flask was supplemented with 0.1% chloramphenicol 1 h prior to harvesting. To separate
434 the moisture from the mycelia, the culture was filtered through muslin. The dry mycelia were
435 transferred to a pre-cooled mortar and pestle to lyse the cells. All further operations were per-
436 formed at 4°C. The cells were lysed using sea-sand (silicon dioxide) and SEMP buffer (250 mM
437 sucrose, 1 mM ethylenediaminetetraacetic acid (EDTA), 10 mM MOPS-KOH pH 7.2, 2 mM
438 phenylmethanesulfonyl fluoride (PMSF), and 0.2% chloramphenicol), by applying a 20 min
439 grinding course. Sand and cell debris were removed using differential centrifugation at low-speed
440 (2000 x g). A subsequent high-speed centrifugation step (17,500 x g) was carried out to sediment
441 crude mitochondria. The mitochondrial pellet was then resuspended in SEM buffer (250 mM su-
442 crose, 1 mM EDTA, and 10 mM MOPS-KOH pH 7.2). To further purify, the crude mitochondria
443 were undergone a sucrose gradient in SEM buffer for 1h at 28,000 rpm with an SW40 Ti rotor
444 (Beckman Coulter). Mitochondrial band was pooled and stored at -80 °C.

445 Mitochondria were lysed in 4 volumes of lysis buffer (25 mM Hepes-KOH pH 7.5, 20 mM KCl,
446 15 mM $Mg(OAc)_2$, 2% *n*-dodecyl-β-D-maltoside (DDM), 0.0075 % cardiolipin, 2 mM dithio-
447 threitol (DTT), 1 tablet of protease inhibitor (cOmplete™, Roche), and RNase inhibitor
448 (RNaseOUT, Invitrogen)) and incubated for 5 min at 4°C. The membrane was separated by cen-
449 trifugation of the mitochondrial lysate at 30,000 x g for 20 min followed by a second centrifuga-
450 tion step with the same settings. The supernatant was loaded onto a 1.0 M sucrose cushion in the
451 resuspension buffer (20 mM Hepes-KOH pH 7.5, 15 mM KCL, 15 mM $Mg(OAc)_2$, 0.05% DDM,
452 0.0075% cardiolipin, and 2 mM DTT) with RNase inhibitor and centrifuged at 48,000 rpm with a
453 70 Ti rotor for 4 h. The pellet was then resuspended in the resuspension buffer, loaded on a 15-
454 30% sucrose gradient in the resuspension buffer, and centrifuged at 23,000 rpm with an SW40 Ti
455 for 16 h at 4°C. Fractions containing mitoribosomes were collected and the mitorobosomes were
456 pelleted by centrifugation at 100,000 rpm with a TLA120.2 rotor (Beckman Coulter) for 45 min
457 at 4°C and resuspended in the resuspension buffer.

458

459 **Cryo-EM and image processing**

460 Freshly purified mitorobosome sample (A_{260} = 3.0) was used for grid preparation. 3 µl aliquots of
461 purified mitoribsomes was incubated for 30 s on glow-discharged holey carbon grids (Quantifoil
462 R2/2, 300 mesh, copper) pre-coated with a home-made continuous carbon film with thickness of
463 ~ 27 Å. The grids were thereafter vitrified in a liquid ethane with a Vitrobot MKIV (FEI/Thermo
464 Fisher) using a blotting time of 3 s at 4°C and 100% humidity. Micrographs were collected with a
465 300 kV Titan Krios (FEI/Thermo Fisher) transmission electron microscope, 70 µm C2 aperture,

using a slit width of 20 eV on a GIF-Quantum energy filter (Gatan). A K2 summit detector (GATAN) was used in the counting mode at the calibrated magnification of 130,000 (yielding a pixel size of 1.06 Å). An exposure time of 9 s yielding a total of 35 e/Å^2 was dose fractionated into 20 frames. In total 3,172 movies were collected automatically during two consecutive days using EPU (FEI/Thermo Fisher) data collection software. Defocus values ranged between 0.8 and 3.0 μm.

Collected movie frames were aligned and corrected for both global and non-uniform local beam-induced movements using MotionCor[34] and the contrast transfer function (CTF) parameters were estimated using Gctf[35], inside the SCIPION program (de la Rosa-Trevín, Quintana et al. 2016). Subsequent data processing steps were performed using RELION-2.1 and 3.0[36]. First, 647 particles were manually picked, followed by two-dimensional (2D) classification. Four good 2D class averages were used for reference-based picking for the second round. 265,710 picked particles were subjected to 2D classification and 50 good 2D classes were selected (Figure S1A). Retained 223,605 particles were classified into six classes by three-dimensional (3D) classification, resulted in four good mito-monosome classes (131,806 particles), one class with weak mtSSU density (36,053 particles), and one low quality class containing junks. From the class with weak mtSSU density, isolated mtLSU particles (24,142 particles) are classified out by further 3D classification.

Pooled good particles were subjected to 3D auto-refinement. Per-particle CTF refinement[37], followed by Bayesian polishing[38] and the second round of per particle CTF refinement to improve resolution, resulted in reconstructions of mito-monosome and the isolated mtLSU with 2.83 and 3.03 Å resolution, respectively (Figure S1A). Resolution is estimated based on the gold standard criterion of Fourier shell correlation (FSC) = 0.143 between the reconstructed two half maps.

Due to the relative movement between the mtSSU and mtLSU in monosome, we suffered from low resolution in the mtSSU. We therefore decided to improve the quality of the maps by focused masked refinement for the mtSSU and mtLSU separately. We obtained the masked maps of mtLSU and mtSSU with 2.74 and 2.85 Å resolution, respectively. Further, improvement of local resolutions was achieved by focused refinement using the local masks as described in the Supplementary Material.

All the density maps were locally resolution filtered by applying a negative B-factor estimated automatically by RELION-3.0.

The observed motion between mtLSU and mtSSU prompted us to separate possible sub-states of the monosome. Firstly, we classified the particles in two major classes (ratcheted and non-ratcheted states) by overall 3D classification. To facilitate classifying tRNA states, signal subtraction of ribosome was performed using a cylindrical mask covering the A-, P-, and E-sites for the ratcheted and non-ratcheted states separately by RELION 3.0, following by focused 3D classification without alignment. For the ratcheted state, the same cylindrical mask was applied for the classification, which separated the P/E hybrid tRNA bound mitoribosomes (37,908 particles). For non-ratcheted state, smaller masks were needed to classify tRNAs. The P/P tRNA bound mitoribosomes were separated applying a mask covering only the P-site, while E/E tRNA bound ones were separated by a mask covering only the E-site. The P/P tRNA and E/E tRNA

506 bound mitoribosomes were 24,611 and 23,802 particles, respectively. Among them, only 4,136
507 particles are overlapping and have both P/P and E/E tRNAs, which are too few for high-
508 resolution reconstruction. Local resolution of the tRNA bound mitoribosomes were also
509 improved by using local masked refinement as described in the Supplementary Material.
510

511 **Model building and refinement**

512 Model building was carried out in Coot[39]. Rigid body docking was carried out in UCSF
513 Chimera[40]. The model of the *S. cerevisiae* mitoribosome (PDB ID: 5MRC) was used as a refer-
514 ence. For proteins whose orthologs existed in *S. cerevisiae* structure, the homology models of *N.*
515 *crassa* were generated by SWISS Model[41], placed into the density, manually revised and built
516 unmodeled and unique regions, and real space fit in Coot. Previously unknown or unmodeled
517 proteins were modeled *de novo* in Coot. For the correct assignment of the proteins, sequence
518 stretches of reasonable quality were directly identified from the map and then applied to
519 BLAST[42] and/or compared to the protein sequences gained from mass spectrometry. The riboso-
520 mal protein mL108 was named according to the standard nomenclature widely accepted in the
521 ribosome community[43]. The number was chosen in a chronological order of discover also consid-
522 ering unpublished data. The entire rRNAs, tRNAs, and mRNAs were modeled *de novo* in Coot.
523 Since bound tRNAs and mRNAs are mixture of any mitochondrial ones, each residue was as-
524 signed as either A, U, G, or C, based on the density and conservation. Ligands and metal ions
525 were placed into the density.

526 For model refinement of the consensus mtLSU and mtSSU and the monosomes in the three tRNA
527 states, the local masked refined maps with B-factor sharpening and local-resolution filtering were
528 merged using the program phenix_combine_focused_maps in the Phenix software suite [44], there-
529 by generating a map for model refinement. For the isolated mtLSU, the overall refined map with
530 B-factor sharpening and local-resolution filtering was used for model refinement. Refinement of
531 all models was performed using Phenix.rel_space_refine[45]. The final structure was validated us-
532 ing the MolProbity[46] implementation of the Phenix suite.
533

534 **Figure preparation**

535 All structural figures were generated with PyMOL[47], UCSF Chimera[40], and ChimeraX[48]. The
536 secondary structure diagrams of the 16S and 23S rRNA were generated using XRNA
537 (http://rna.ucsc.edu/rnacenter/xrna/xrna.html).
538

539 **Acknowledgements** We thank Frank Nargang for providing the *N. crassa* strain, and Marta
540 Carroni and Julian Conrad for supporting cryo-EM data collection. The data was collected at the
541 SciLifeLab cryo-EM facility funded by the Knut and Alice Wallenberg, Family Erling Persson,
542 and Kempe foundations. Mass spectrometry analysis was performed by the Clinical Proteomics
543 Mass Spectrometry facility, Karolinska Institutet/ Karolinska University Hospital/ Science for
544 Life Laboratory. This work was supported by the Swedish Foundation for Strategic Research
545 (FFL15:0325), Ragnar Söderberg Foundation (M44/16), Swedish Research Council (NT_2015-

546 04107), Cancerfonden (2017/1041), European Research Council (ERC-2018-StG-805230), Knut
547 and Alice Wallenberg Foundation (2018.0080), EMBO Young Investigator Program. Y.I. is
548 supported by H2020-MSCA-IF-2017 (799399-Itohribo).

549

550 **Author contributions** A.A. designed the project. N.M prepared the sample and collected cryo-
551 EM data. Y.I., A.N. and N.M. processed the data and built the model. A.N. and A.A. wrote the
552 manuscript with help from Y.I., N.M. and J.H.

553

554 **Competing interests** The authors declare no competing interests.

555

556 Supplementary Information for

557 **Analysis of translating mitoribosome reveals functional characteristics of**
558 **protein synthesis in mitochondria of fungi**

559

560 Yuzuru Itoh[1,2†], Andreas Naschberger[1†], Narges Mortezaei[1†], Johannes Herrmann[3]
561 and Alexey Amunts[1,2]*

562

563 [1]Science for Life Laboratory, Department of Biochemistry and Biophysics, Stockholm
564 University, 17165 Solna, Sweden

565 [2]Department of Medical Biochemistry and Biophysics, Karolinska Institutet, 17165
566 Solna, Sweden

567 [3]Cell Biology, University of Kaiserslautern, Erwin-Schrödinger-Straße 13, 67663 Kaiserslautern,
568 Germany

569 † These authors contributed equally to this work.

570

571

572 *Correspondence and request for material should be addressed to amunts@scilifelab.se

573

574

575 **This file includes:**

576 Supplementary Figures 1-11

577 Supplementary Tables 1-2

578

Supplementary Figures

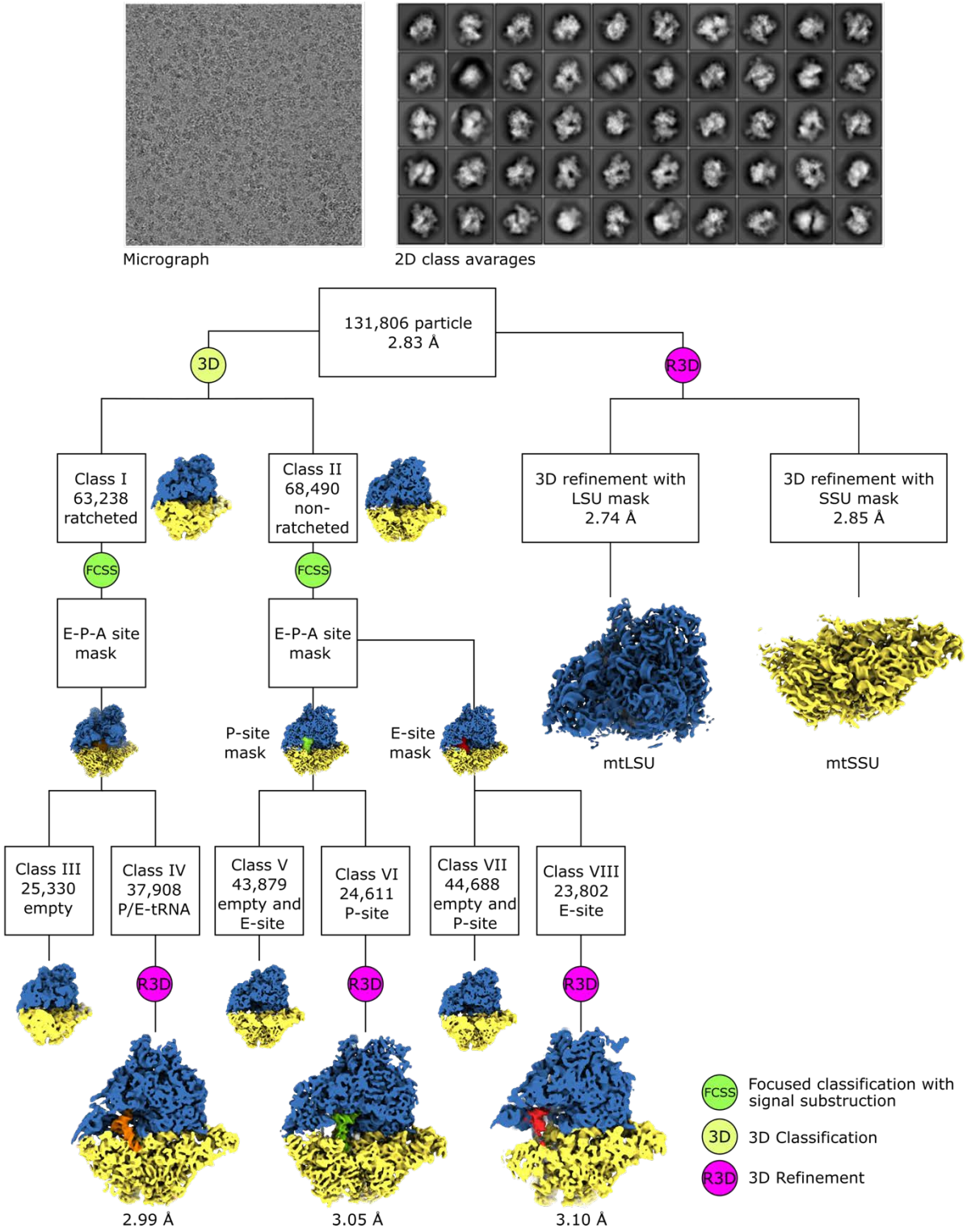

Supplementary Figure 1. Cryo-EM data collection and processing scheme. Representative micrograph and 2D class averages. Data refinement protocol and classification scheme for mtLSU, mtSSU and monosome in three tRNA bound states.

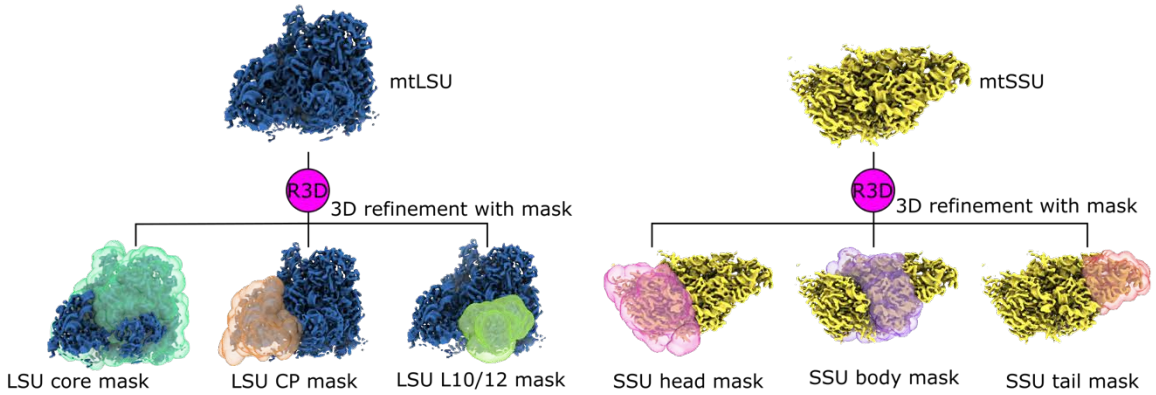

584

585 **Supplementary Figure 2. Masked refinement of mitoribosomal subunits.** Masks for mtLSU
586 core, CP, L7/12 stalk; mtSSU head, body, tail were used to improve the density locally.

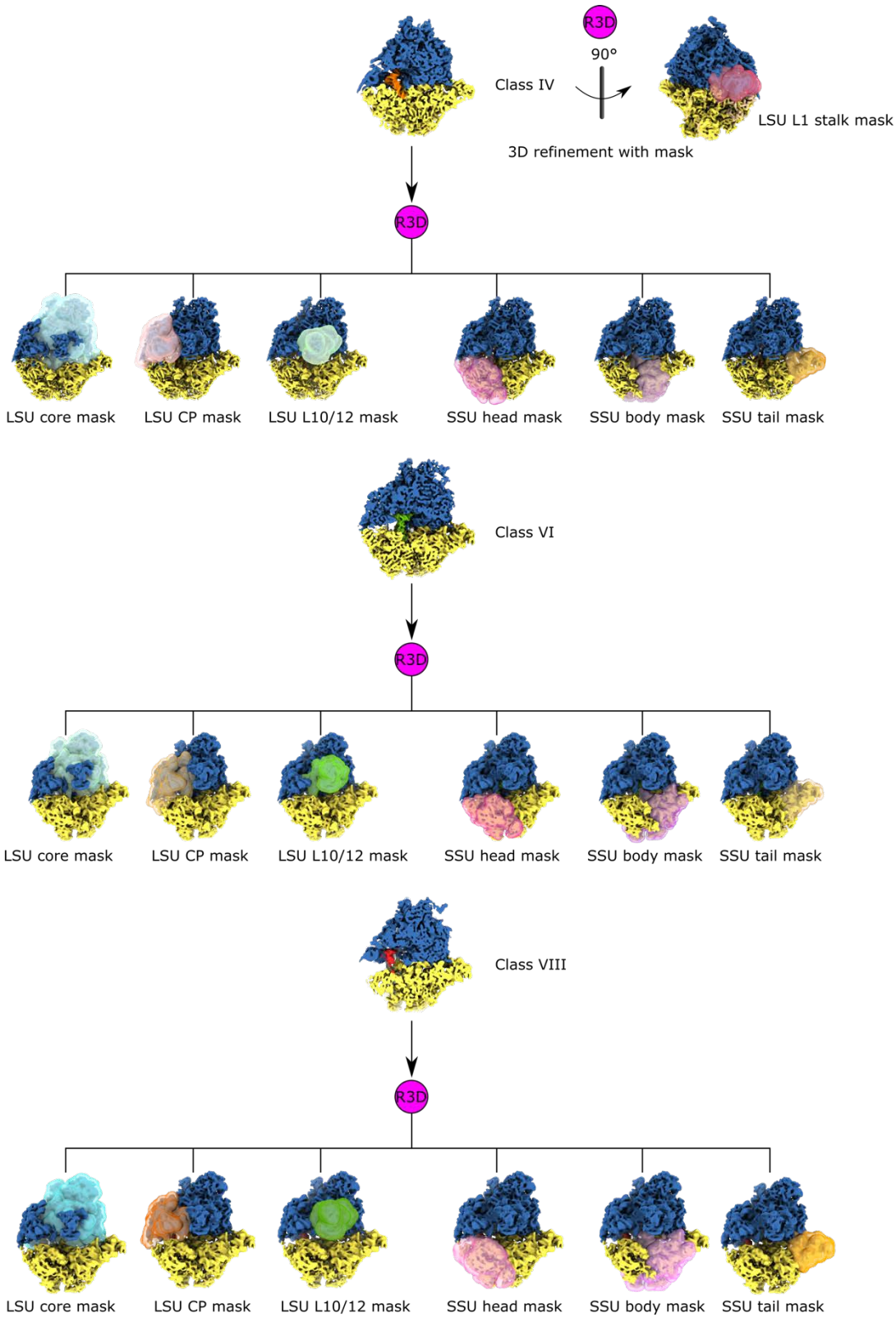

587

588 **Supplementary Figure 3. Masking refinement of the mitoribosomes in tRNA bound states.**

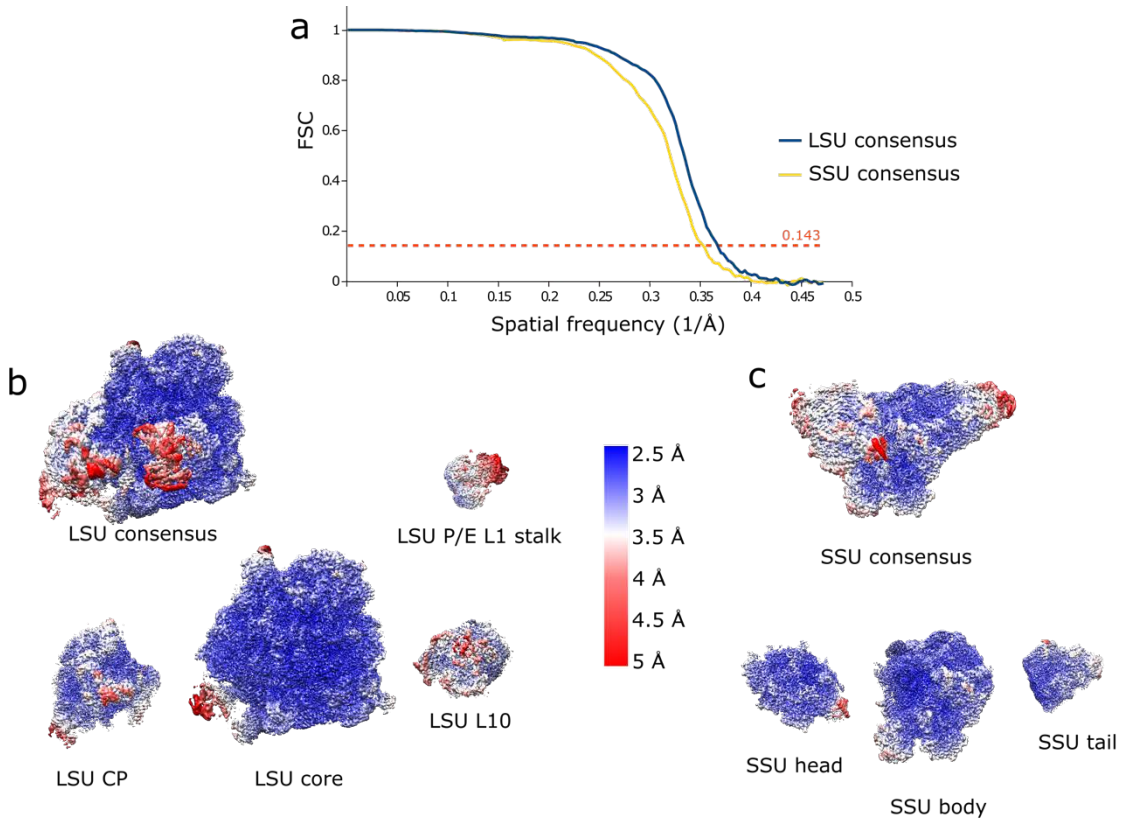

Supplementary Figure 4. Overall and local resolution estimations of mitoribosomal subunits. a, Fourier Shell Correlation (FSC) curves for the refined maps of mtLSU and mtSSU. Value of 0.143 is indicated. **b,** mtLSU cryo-EM maps viewed according to local resolution. **c,** mtSSU cryo-EM maps viewed according to local resolution.

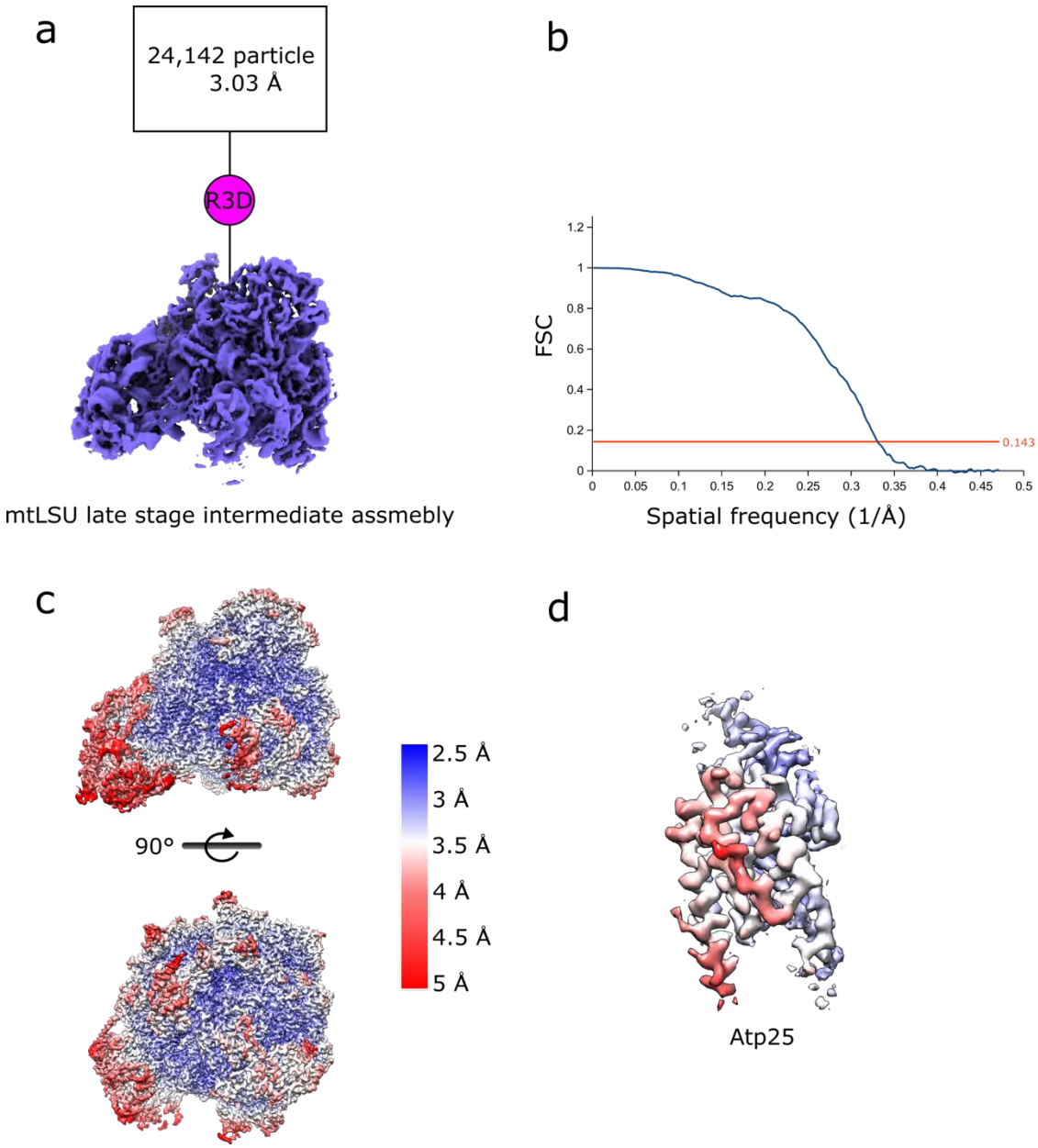

Supplementary Figure 5. Data processing and overall and local resolution estimations of mtLSU-Atp25 assembly intermediate. a, Processing scheme. **b,** Fourier Shell Correlation (FSC) curves for the refined map. Gold standard value of 0.143 is indicated. **c,** mtLSU-Atp25 assembly intermediate cryo-EM maps colored according to local resolution. **d,** Zoomed in map for Atp25 colored by local resolution.

603

604 **Supplementary Figure 6. Structure-based secondary structure diagram of the mtLSU rRNA.** Expansion segments shared between
605 *N. crassa* and *S. cerevisiae* are highlighted with red, specific expansion segments are highlighted with yellow. Those present in *S.*
606 *cerevisiae* only are indicated by light blue arrows. rRNA somains are labeled with roman numerals.

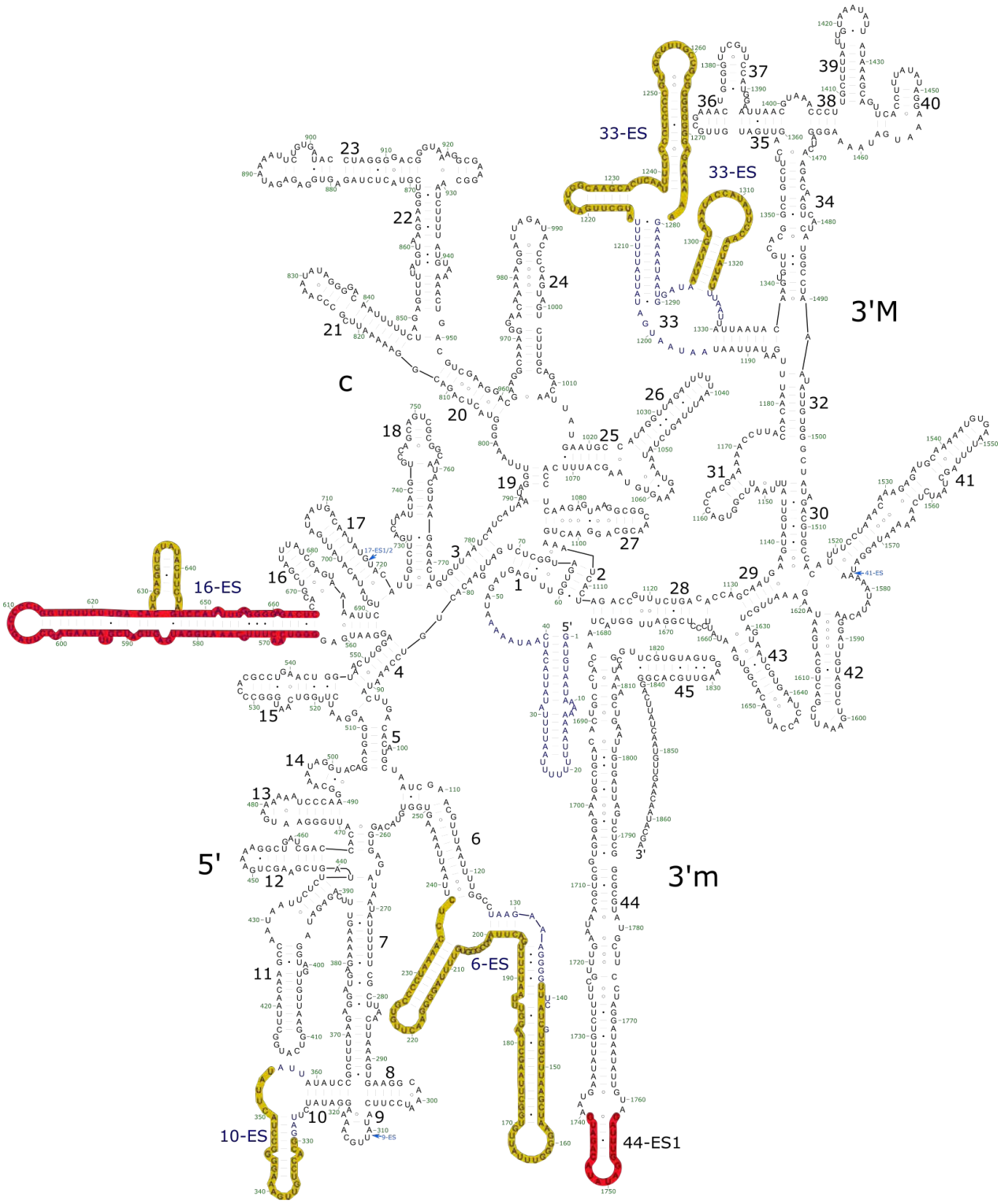

Supplementary Figure 7. Structure-based secondary structure diagram of the mtLSU rRNA. Expansion segments shared between *N. crassa* and *S. cerevisiae* are highlighted with red, specific expansion segments are highlighted with yellow. Those present in *S. cerevisiae* only are indicated by light blue arrows. rRNA domains are labeled with roman numerals.

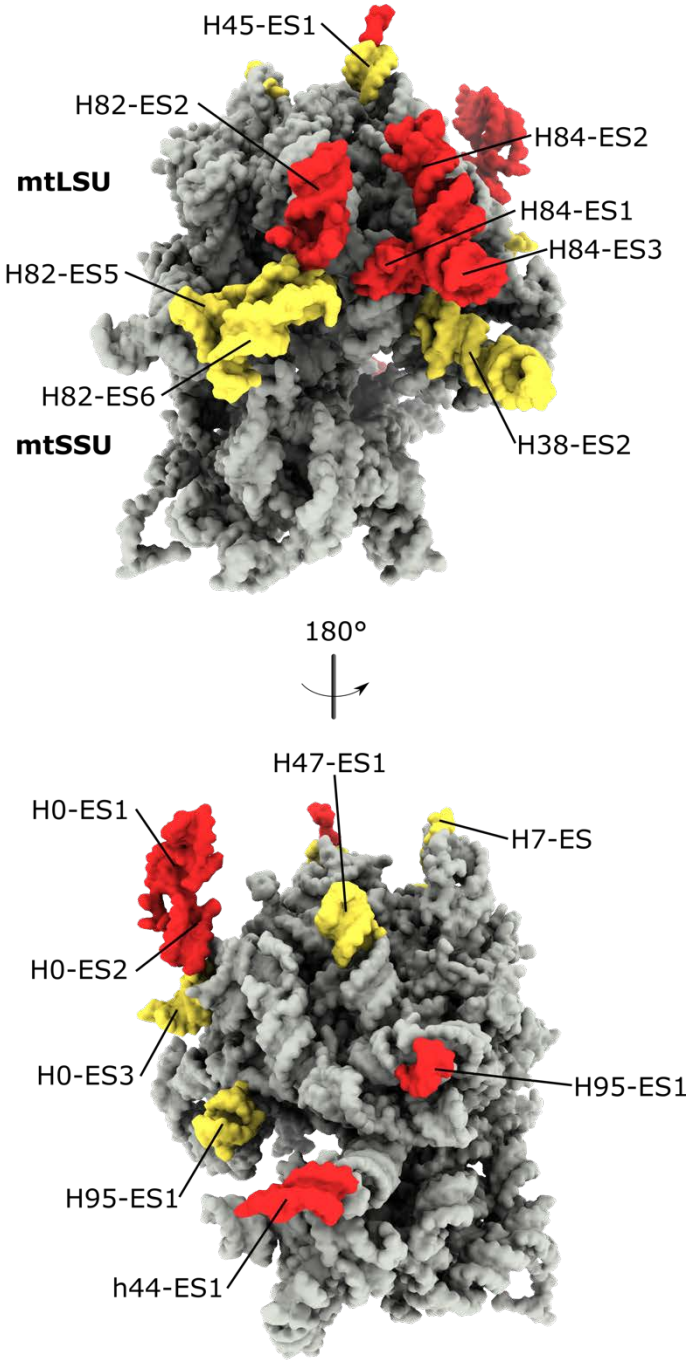

Supplementary Figure 8. 3D view of the rRNA of mtLSU and mtSSU. The conserved rRNA is in gray. ESs shared with *S. cerevisiae* are in red, and specific ESs in yellow.

616

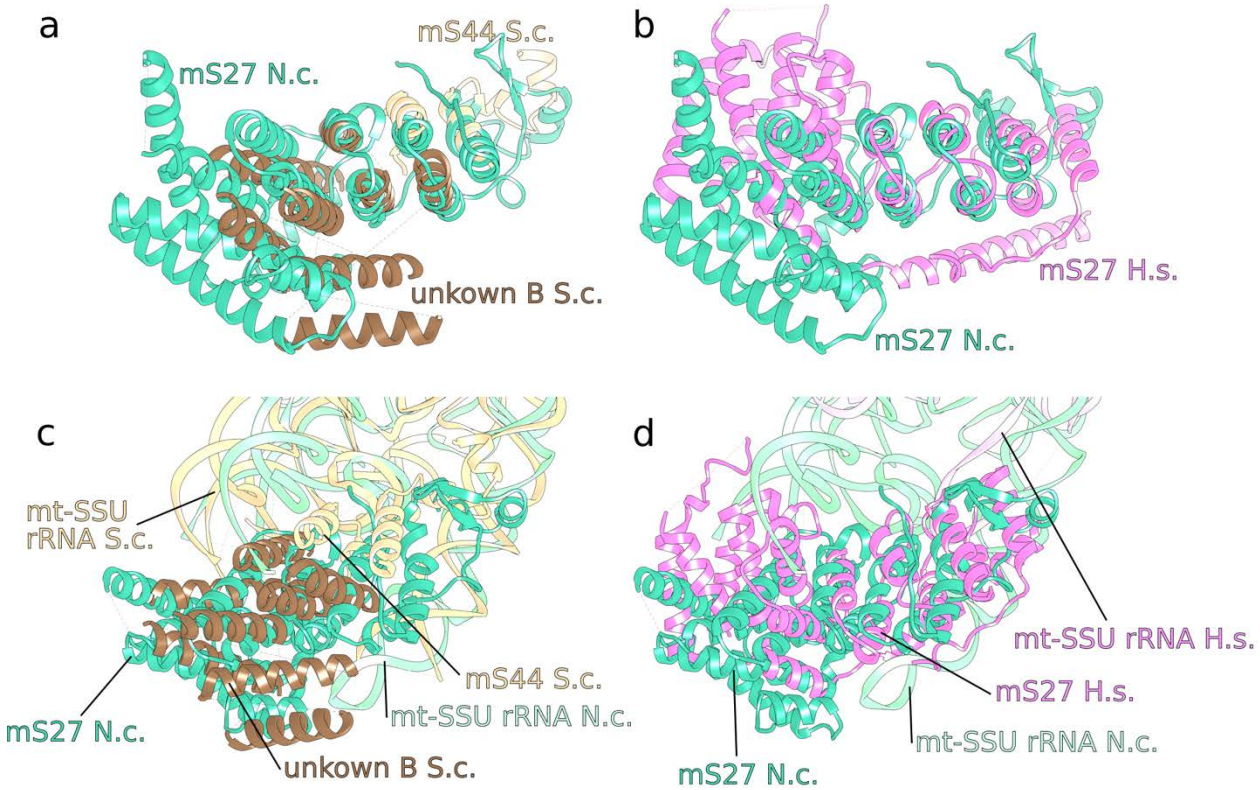

617

618 **Supplementary Figure 9. Superposition of mS27 orthologs. a,** *N. crassa* and *S. cerevisiae*
619 mS27 is superimposed (previously assigned as mS44, 'unknown B'). **b,** *N. crassa* and *H. sapiens*
620 mS27 is superimposed, showing similar fold. **c,** Superposition based on mtSSU rRNA suggests
621 the same location form mS27 from *N. crassa* and *S. cerevisiae*. **d,** Superposition based on mtSSU
622 rRNA suggests the same location form mS27 from *N. crassa* and *H. sapiens.*

623

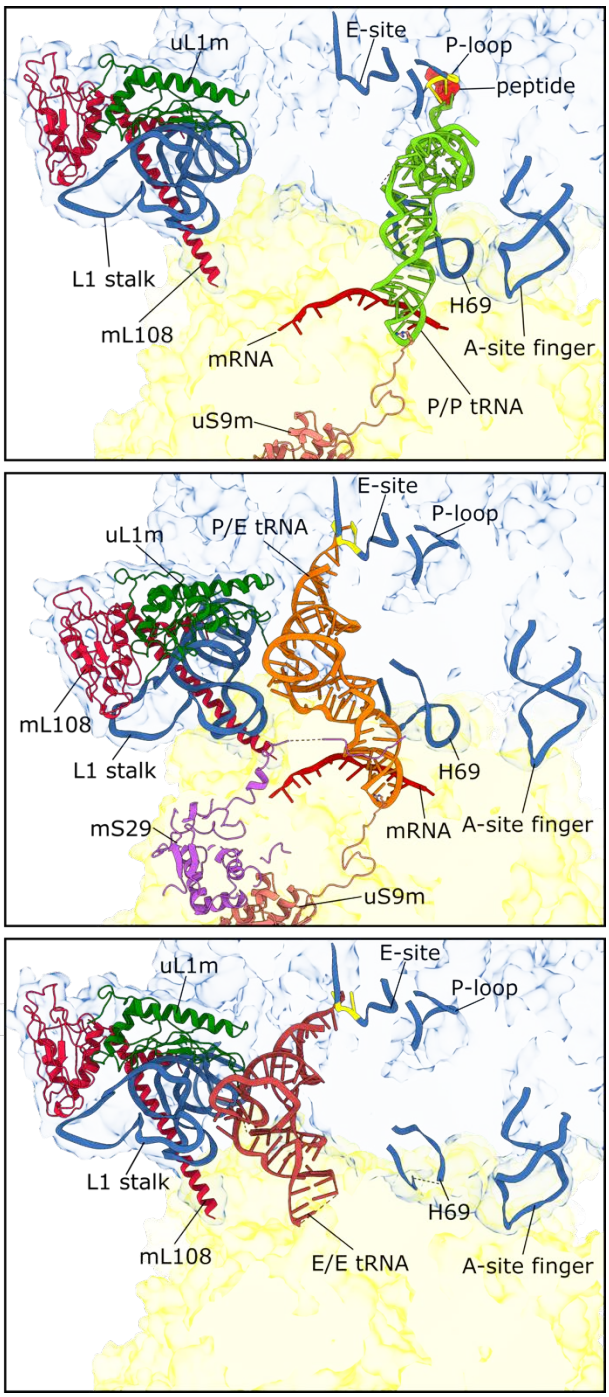

Supplementary Figure 10. The L1-stalk and translocation of tRNA. The three states are structurally aligned on mtLSU. Transparent surfaces of mtLSU and mtSSU are colored in blue and yellow respectively. Cartoon representations of important parts are shown and labeled. The P/P-tRNA state with the tRNA colored in green (top panel). The P/E-tRNA state with the tRNA colored in orange (middle panel). The E/E-tRNA state with the tRNA colored in red (bottom panel).

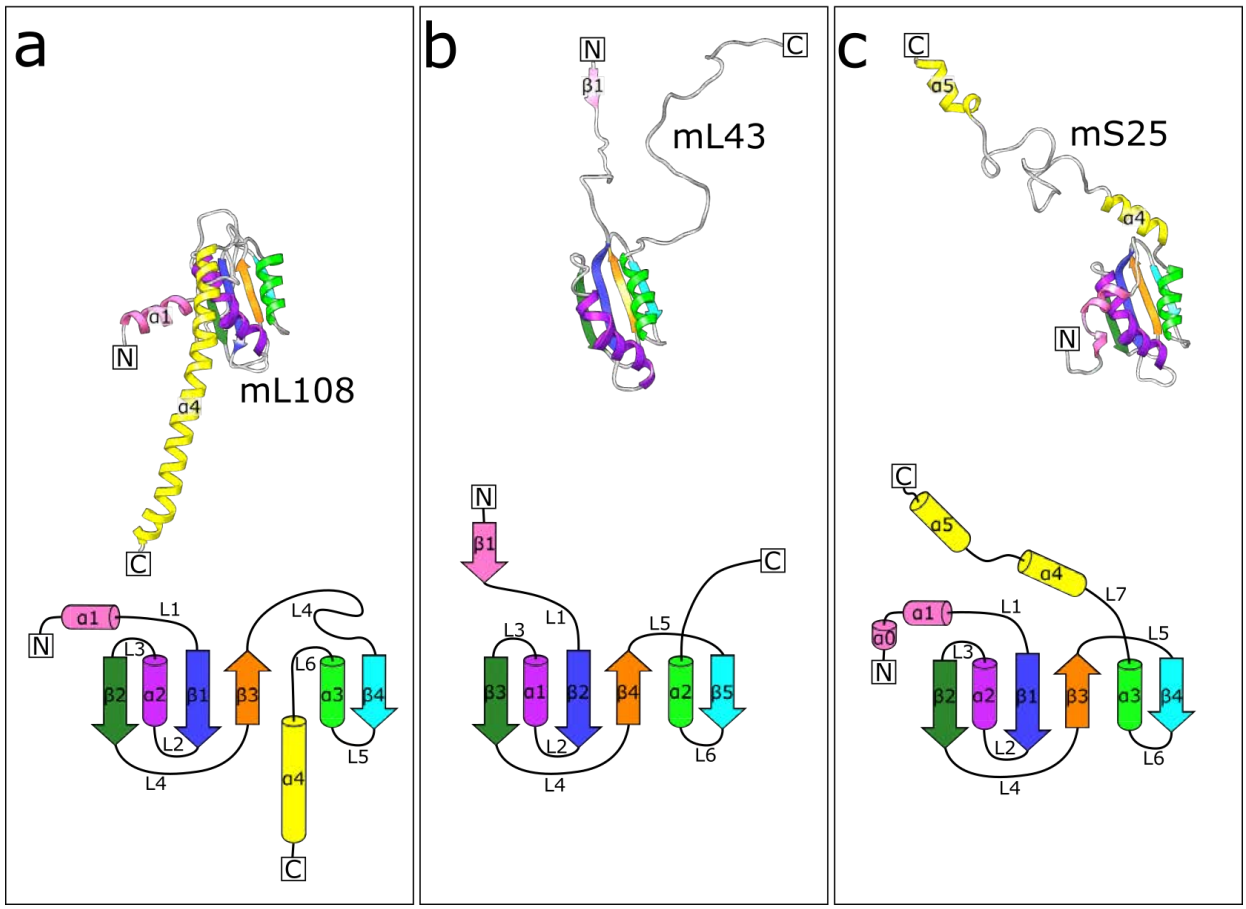

Supplementary Figure 11. Structural topologies of mL108 and its homologs. Secondary structures are colored and labeled from the N- to C-termini. In the topology α-Helices and β-strands are shown as cylinders and arrows respectively and match the colors of the secondary structural elements in the cartoon representation. The structures of **a,** mL108 of *N. crassa*. **b,** mL43 of *N. crassa* and **c,** mS25 of *S. scrofa* (PDB ID: 5AJ4) are shown side by side to highlight their structural similarity.

640 # Supplementary Tables

641 ## Supplementary Table 1. List of RNA and proteins from mtLSU.

Name	Gene	Uniprot ID	Chain ID	Modeled	Size	Notes
23S rRNA	–	–	A		3464	Spermine bound next to A1271.
uL1m	MRPL1	Q1K699	e	59–300	303	Conserved in *S. cerevisiae* and human but disordered in their structures.
uL2m	RML2	Q7SCX7	B	54–379	383	Likewise its *S. cerevisiae* counterpart, NT extension locates at the subunits interface.
uL3m	MRPL9	Q1K8T6	C	63–369	384	A helix at CT extension is similar to the human uL3m. This extension does not exist in the *S. cerevisiae* counterpart.
uL4m	YML6	V5IMN1	D	62–302, 312–324	325	
uL5m	MRPL7	Q1K6P0	E	44–352	352	
uL6m	MRPL6	Q7RZF0	F	52–252	255	
bL9m	MRPL50	Q7S054	G	52–125	300	
uL10m	MRPL11	Q7RZ62	f	54–298	347	Conserved in *S. cerevisiae* and human. It is not modeled in the *S. cerevisiae* structures.
uL11m	MRPL19	Q7RX40	g	12–158	158	Conserved in *S. cerevisiae* and human. It is not modeled in the *S. cerevisiae* structures.
uL13m	MRPL23	Q7SBV6	H	1–183	183	
uL14m	MRPL38	Q7SBJ8	I	1–46, 59–130	131	
uL15m	MRPL10	Q7SB98	J	47–289	312	
uL16m	MRPL16	F5HIJ5	K	61–228	249	
uL17m	MRPL8	Q1K8C8	L	2–193	193	CT extension unlike its *S. cerevisiae* counterpart lacking a helix.
bL19m	IMG1	Q7RYW8	M	41–234	258	
bL21m	MRPL49	Q7SGE5	N	85–217	217	
uL22m	MRPL22	Q7S5N0	O	43–71, 122–364	364	NT extension extensively remodeled with respect to its *S. cerevisiae* counterpart, whereas CT extension is quite similar. NT partially occupies the position of the absent bacterial rRNA helix 24.
uL23m	MRP20	Q7SA60	P	13–192	228	CT extension remodeled respective to its *S. cerevisiae* counterpart. Most likely it does not block the bacterial exit tunnel likewise CT extension in *S. cerevisiae* uL23m.
uL24m	MRPL40	Q7RXU7	Q	1–353	396	NT extension is a long helix that is not like its bacterial, *S. cerevisiae*, and human counterparts. CT extension is similar to that of the *S. cerevisiae*; it covers a long distance through the surface thereby connecting different parts of the large subunit. The CT extension compensates the absence of bacterial helices 15 and 16.
bL27m	MRP7	Q1K730	R	75–196, 248–383	447	NT extension is similar to bacterial, *S. cerevisiae* and human counterparts. CT extension extensively remodeled respective to *S. cerevisiae* bL27, and partially interacts with rRNA helix 82.
bL28m	MRPL24	Q7SC44	S	42–203, 209–225	274	CT extension remodeled extensively respective to *S. cerevisiae* counterpart.
uL29m	MRPL4	Q7S910	T	44–223	263	
uL30m	MRPL33	Q1K8Y7	U	2–102, 125–161	161	
bL31m	MRPL36	Q1K7L7	V	48–128, 189–207	219	Bridging the LSU CP and the SSU head.
bL32m	MRPL32	Q1K4P1	W	64–122	129	Zn binding

bL33m	MRPL39	V5IM60	X	7–54	59	
bL34m	MRPL34	Q96U95	Y	95–140	140	
bL36m	RTC6	Q7S4E7	0	79–124	124	Zn binding
mL38	MRPL35	Q7RXV8	1	83–449	449	CT extension partially compensates the absence of bL35. Stabilizes helices 84-ES and 82-ES.
mL40	MRPL28	V5IQE0	2	251–370	370	Stabilize helices 82-ES, 84-ES, 38-ES1. NAD is binding and interacting with mL40
mL41	MRPL27	Q7S5W0	3	9–103	103	
mL43	MRPL51	Q7S300	4	2–138	138	
mL44	MRPL3	Q7SA88	5	55–235 273-439	439	NT extension slightly remodeled respective to *S. cerevisiae* mL44. CT extension interacts with helix 0-ES1. It forms heterodimer with mL57.
mL46	MRPL17	Q7S1Z3	6	81–245 253-303 311-368	368	Interacts with helices 38-ES1 and 82-ES.
mL49	IMG2	Q7S518	7	82–165	165	Most likely interacts with helix 28.
mL50	MRPL13	Q7S711	8	273–296, 303–442	443	Extensively remodeled. A 31 amino-acid long helix at the solvent-exposed surface of the protein. Interacting with helices 45 and 46.
mL53	MRPL44	Q7SGH0	h	1–98	98	Conserved in *S. cerevisiae* and human. It is not modeled in the *S. cerevisiae* structures.
mL54	MRPL37	Q7SCZ3	i	77–118, 138–218	218	Bridges L10/L11 area to CP. Conserved in *S. cerevisiae* and human. It is not modeled in the *S. cerevisiae* structures and only one helix is modeled in the human structures.
mL57	MRPL15	Q7S1R6	9	61–265	267	Forms a heterodimer with mL44. Stabilizes helix 0-ES1.
mL58	MRPL20	Q1K6U7	a	41–103, 129–225	225	Interacts with helix 0.
mL59	MRPL25	Q7SEK9	b	2–162	162	
mL60	MRPL31	U9W8F2	c	13–110	110	
mL67	MHR1	Q7RYM5	d	33–218 243-291	292	Similar to its *S. cerevisiae* counterpart with slight remodeling at NT and CT extensions.
mL108	MRPL49	Q7RWZ7	j		201	Conserved but not modeled in *S. cerevisiae*
Nascent polypeptide	-	-	XX			

644 **Supplementary Table 2. List of RNA and proteins from mtSSU.**

MRP	Gene	Uniprot ID	Chain ID	Modeled	Size	Notes
16S rRNA	–	–	a		1864	
bS1m	MRP51	A7UWX2	A		470	
uS2m	MRP4	V5ILE0	B		428	
uS3m	VAR1	P23351	C		508	
uS4m	NAM9	Q7SA90	D		453	
uS5m	MRPS5	Q1K548	E		477	Has a unique insertion to form a unique second beak.
bS6m	MRP17	Q7SB95	F	2–117	117	
uS7m	RSM7	Q7S6M9	G		309	
uS8m	MRPS8	Q7SHF3	H	2–161	161	
uS9m	MRPS9	Q7S7R6	I		315	
uS10m	RSM10	Q7RYL4	J		268	
uS11m	MRPS18	Q7SGU0	K		376	
uS12m	MRPS12	Q7S9I4	L		174	
uS13m	SWS2	Q7S2C2	M	2–119	119	
uS14m	MRP2	Q7SF85	N	2–113	113	
uS15m	MRPS28	Q1K5G1	O		320	
bS16m	MRPS16	P08580	P		107	
uS17m	MRPS17	Q7S4E0	Q		165	A unique C-terminal helix, which binds the ATP IF_1 dimer.
bS18m	RSM18	Q1K8E0	R		256	
uS19m	RSM19	Q1K8V2	S		91	
bS21m	MRP21	Q7SAJ1	T		236	
mS23	RSM25	F8MRK5	U		240	
mS26	PET123	Q7SHR9	V		316	
mS27	MRP13	Q7RYW7	W		396	Corresponds to mS27 in human. *S. cerevisiae* mS44 and the unknown B (PDB ID: 5MRC) are one connected protein, which corresponds to human and *N. crassa* mS27.
mS29	RSM23 /DAP3	Q7SD06	X		469	DAP3 death associated protein 3. ATP and Mg ion are bound.
mS33	RSM27	Q1K5R0	Y		108	
mS35	RSM24	Q1K5Z0	Z		382	Has a unique N-terminal domain to form a unique beak.

mS37	MRP10	Q7S4Y4	1	2–89	90	
mS38	COX24	Q7SHR6	2	312–344	344	
mS41	FYV4	Q1K6Q3	3		236	
mS42	RSM27 /MRP1	Q7S2H6	4, 5		310	Homolog of Fe superoxide dismutase. Lost the catalytic Fe ion binding side. Two chains form a homodimer, in contrast to the mS42-mS43 heterodimer in *S. cerevisiae*.
mS45	MRPS35	Q7SHB2	6		348	
mS46	RSM28	Q7SG49	7		414	
mS47	MRP5 /EHD3	Q1K7A4	8		508	3-hydroxyisobutyryl-CoA hydrolase. Probably an active enzyme because its active site is conserved.
ATPIF1	INH1	V5IRA3	0, 9		95	ATP synthase inhibitor 1. Forms a homodimer located in the SSU tail region.
tRNA	–	–	b		76	P, E or P/E tRNA state. The density is mixture of tRNA species.
mRNA	–	–	e		–	

645